Journal of Materials Chemistry B

Combinatorial microneedle patch with tunable release kinetics and dual fast-deep/sustained release capabilities

Journal:	*Journal of Materials Chemistry B*
Manuscript ID	TB-COM-01-2021-000141.R1
Article Type:	Communication
Date Submitted by the Author:	11-Feb-2021

Complete List of Authors:	Lopez-Ramirez, Miguel; University of California San Diego, Department of Nanoengineering Kupor, Daniel; University of California San Diego, Nanoengineering Marchiori, Leonardo; University of California San Diego, Nanoengineering Soto, Fernando; University of California San Diego, Department of NanoEngineering Rueda, Ricardo; University of California San Diego, Nanoengineering Reynoso, Maria; University of California San Diego Narra, Lakshmi; University of California San Diego Chakravarthy, Krishnan; University of California San Diego Department of Anesthesiology Wang, Joseph; University of California San Diego, Department of Nanoengineering

Combinatorial microneedle patch with tunable release kinetics and dual fast-deep/sustained release capabilities

Miguel Angel Lopez-Ramirez,[a] Daniel Kupor,[a] Leonardo Marchiori,[a] Fernando Soto,[a] Ricardo Rueda,[a] Maria Reynoso,[a] Lakshmi Rekha Narra,[b] Krishnan Chakravarthy*[a,b] and Joseph Wang*[a]

[a] Department of Nanoengineering, University of California, San Diego, La Jolla, California 92093, United States.
[b] Department of Anesthesiology and Pain Medicine, University of California, San Diego, Health Sciences, La Jolla, California, 92093, United States.

* Correspondence to: kvchakravarthy@health.ucsd.edu and josephwang@ucsd.edu

Abstract

Transdermal microneedle (MN) drug delivery patches, comprising water-soluble polymers, have played an essential role in diverse biomedical applications, but with limited development towards fast deep release or sustained delivery applications. The effectiveness of such MN delivery patches strongly depends on the materials from which they are constructed. Herein, we present a dual-action combinatorial programmable MN patch, comprising of fast and sustained-release MN zones, with tunable release kinetics towards delivering a wide range of therapeutics over different timeframes in single application. We demonstrate the fine tuning of MN materials; the patches can be tailored to deliver a first payload faster and deeper within minutes, while simultaneously delivering a second payload over long times ranging from weeks to months. The active and rapid burst release relies on embedding biodegradable Mg microparticle 'engines' in dissolvable MNs while the sustained release is attributed to biocompatible polymers that allow prolonged release in a controllable tunable manner. In addition, the patches are characterized and optimized for their design, materials and mechanical properties. These studies indicate that such programmable dual-action versatile MN platform is expected to improve therapeutic efficacy and patient compliance, achieving powerful benefits by single patch application at low manufacturing cost.

Introduction

Advanced microfabrication methods have enabled the development of microneedle (MN) arrays as novel transdermal drug-delivery devices,[1,2] that are widely used for treating diverse disease conditions ranging from superficial dermatitis to diabetes and chronic pain.[3-7] MNs are microscale structures that allow the delivery of drugs within few microns of the skin and are considered minimally invasive with minimal patient-reported pain compared to traditional hypodermic needles,[8-11] requiring minimal training from medical practitioners,[12,13] avoiding the cold chain (refrigeration, storage) and are thus suitable for application in remote locations. Optimal design of MN balances various parameters that determine the drug delivery efficiency, mechanical strength, or manufacturability. Currently, MN patches play an essential role in a wide variety of biomedical research applications and are well tolerated in clinical trials,[14,15] leaving behind only biocompatible, dissolvable and hence safe soluble materials when compared to the conventional biohazardous waste left from the needle and syringe. Previous research with MN patches has involved the delivery of small molecules,[16,17] biomacromolecules,[18,19] and nanoparticles (NPs),[20,21] using either coated or non-coated dissolvable MN's,[22,23] usually comprised of highly water-soluble polymer matrixes with narrow development in sustained release applications,[24-30] and limited development in hybrid/programmable MN patches.[31] For example, Nguyen's team recently described core-shell MNs that can deliver cargoes in a pulsatile manner, mimicking release via repetitive bolus injections over long periods of time.[32] Additionally, short-term sustained release microneedles have been reported by employing chitosan,[33] silk fibroin,[34] and PEGDA/PVP[35] polymeric matrices. Nevertheless, each disease has diverse needs and requires different delivery strategies, immediate (fast-acting) or sustained (prolonged) release for over more than a few days. Our ultimate goal is to offer effective post-operative pain management via a fast-local anesthetic delivery for immediate pain relief along with co-delivery of a second anesthetic to address prolonged sustained effects. Consequently, the development of improved, practical and efficient MN patches with tunable dissolution and combinatorial release kinetics, is necessary and required in a wide variety of biomedical applications, as they remain broadly unexplored.[30,36-38]

Herein, we present a dual-action programmable combinatorial MN patch with tunable fast-acting and sustained release of different payloads. The novel dual-action patch was engineered and designed

to have two spatially resolved MN compartments with different dissolution rates and a tunable payload release (Fig. 1). The first compartment (active MNs) made of carboxymethylcellulose (CMC) dissolvable polymer needles allowed a fast and forceful immediate payload release (within ~5 minutes) by incorporating biocompatible and degradable active Mg microparticles. Skin insertion of the fast acting MNs enables instantaneous reaction of the embedded Mg particles with the surrounding interstitial fluid, resulting in the formation of gas (hydrogen) microbubbles, that induce localized vortex flow fields and a 'pumping-like' action within the application site.[39-42] Simultaneously, the nearby second compartment (the sustained MN zone) is made of different concentrations of Eudragit®L100, to allow a controlled and constant sustained payload release over prolonged time periods, ranging from weeks to months. We have demonstrated recently the utility of active Mg-based ballistic MN for effective in vivo melanoma tumor eradication.[37,38] Here we combine such ballistic payload delivery with sustained payload delivery using a single MN patch footprint that offers fast and sustained co-delivery via two neighboring MN compartment zones.

We envision that this fast-acting/sustained release patch will set the foundation for future MN research towards next generation patches, able to treat diverse disease conditions per single application at low manufacturing cost. The ultimate goal of our collaborative research is to apply this unique delivery capability for the management of pain, considering the current limitations of existing pain-relieving patch technologies, such as general Mylan generic lidocaine patches,[43] and the lack of effective transdermal modalities for post-operative settings.[44] Such post-operative pain control will be realized using a single patch, providing fast and slow tunable delivery of the corresponding anesthetic drugs. Yet, the new delivery concept goes beyond pain management as it could greatly benefit broad medical scenarios by delivering different therapeutics with different nature of kinetics and solubility (water soluble in one compartment, while loading a fat-soluble/organic-soluble molecule in the nearby compartment). In the following sections we present the detailed characterization of the new combinatorial MN patch, including its design, fabrication and performance *in vitro* and *ex vivo*.

Results and discussion

Design and fabrication of combinatorial MN patches

The successful realization of the effective combinatorial MN array patch, based on the sequential fast and slow release of different payloads, requires judicious selection and systematic optimization of the materials, design and size to impart the desired biocompatibility and mechanical properties, drug loading capacities and tunable dissolution. The combinatorial MN patch has been engineered to have 2 MN compartment zones, one of which is able to dissolve and rapidly deliver dosages in minutes, while the second zone is slowly dissolved to release its payload over periods ranging from weeks to months (Fig. 1a).

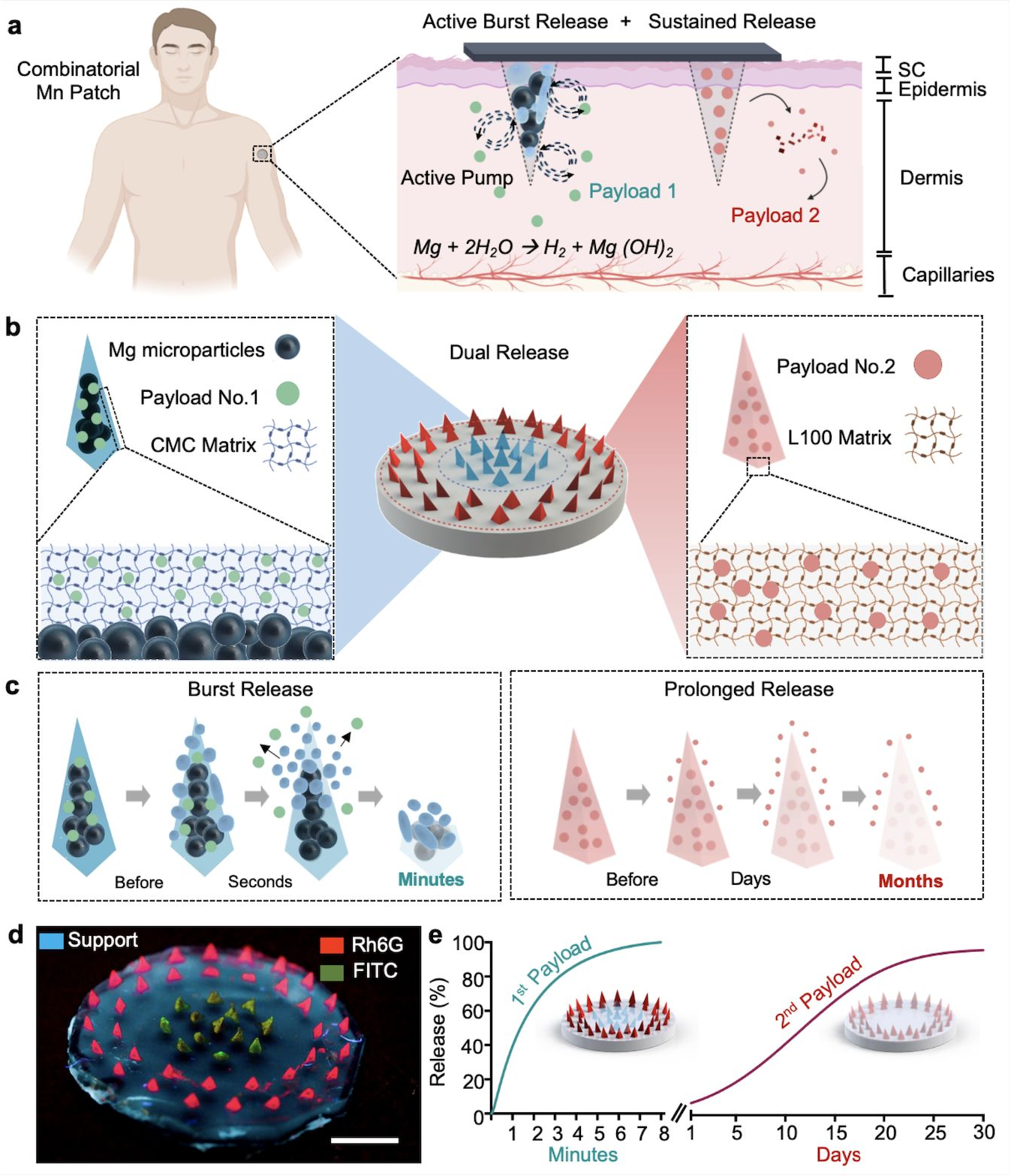

Fig. 1 Combinatorial MN patch with programmable (fast/sustained) drug co-delivery. (a) Schematic illustration of the combinatorial MN patch application process to the skin and dual-stage MN delivery:

fast-acting and sustained release of two payloads. (b) Illustration of the MN patch composition. (c) Time-frame schematics displaying the delivery performance of both compartments: a fast-active burst release of the first therapeutic, along with a prolonged-sustained delivery of a second drug. (d) Digital fluorescence photograph of a combinatorial MN patch displaying both MN compartments loaded with FITC and Rh6G. Scale bar: 2.5 mm. (e) Release kinetics representation of a dual-stage MN patch, featuring the fast delivery of first therapeutic within minutes, while gradually releasing the second drug over weeks and months.

MN compartments were formulated using different materials to meet adequate dissolution and delivery times, and their specific composition was optimized for fine tuning the release kinetics (Fig. 1b). The fast-dissolving MN compartment was formulated using CMC, a water-soluble and safe polysaccharide,[45] with high biocompatibility and biodegradability in the biomedical field, [46,47] often used in biosensors.[48] To facilitate MNs to dissolve instantly and ensure a rapid, forceful payload release from the fast-dissolving compartment we incorporated biocompatible active Mg microparticles within different CMC polymer matrix concentrations. The embedded particles lead to localized generation of gas microbubbles and corresponding vortex flow that results in a nearly instantaneous release of the payload, enabling wider and greater payload distribution and permeation in the application area. Recently, our previous active MN platform was shown extremely useful for eradicating tumor growth in a murine melanoma model, greatly improving immunotherapeutic efficacy.[39,40] The sustained release compartment was designed and formulated of a biocompatible methacrylic acid pH sensitive co-polymer (Eudragit®L100).[49-53] The delivery and release of the sustained MN compartment can be tailored from weeks to months by tuning the polymer concentration used in the fabrication process, therefore obviating the need to load the drug within nanocarriers,[54-56] hence improving the loading. The different dissolution properties and behavior of the combinatorial MN patch (fast-acting and sustained release) are clearly illustrated in Fig. 1c. A characteristic combinatorial MN patch displaying both compartments: fast-acting needles loaded with Fluorescein 5(6)-isothiocyanate (FITC), and prolonged release needles loaded with Rhodamine 6G (Rh6g) is shown (Fig. 1d). Moreover, the release kinetics concept of the dual-stage MN patch, featuring the fast delivery of first payload within minutes, while promoting a gradual-sustained release of the second payload for 30 days is shown in Fig. 1e.

We custom designed and engineered the patch by a mask stereolithography technique (MSLA) with the use of a high-resolution 3D printer. Master MN (triangular right angle shaped) mold dimensions were

designed to be 550µm in base (triangular base length) x 950µm long (height) arranged in a circular pattern (Fig. 2a). The outer compartment comprised of two concentric circular arrays of 35 MNs while the middle compartment of 13 MNs. The base of the array was designed to be 10mm in diameter and 2mm in thickness to ensure facile polydimethylsiloxane (PDMS) micromolding steps. The direct light process (DLP) fabrication projected a 25W UV light source through a 2K LCD masking (XY resolution: 47 µm), photocuring a liquid acrylate resin material in a 20 µm layer-by-layer additive manufacturing fashion (detailed fabrication in experimental section).

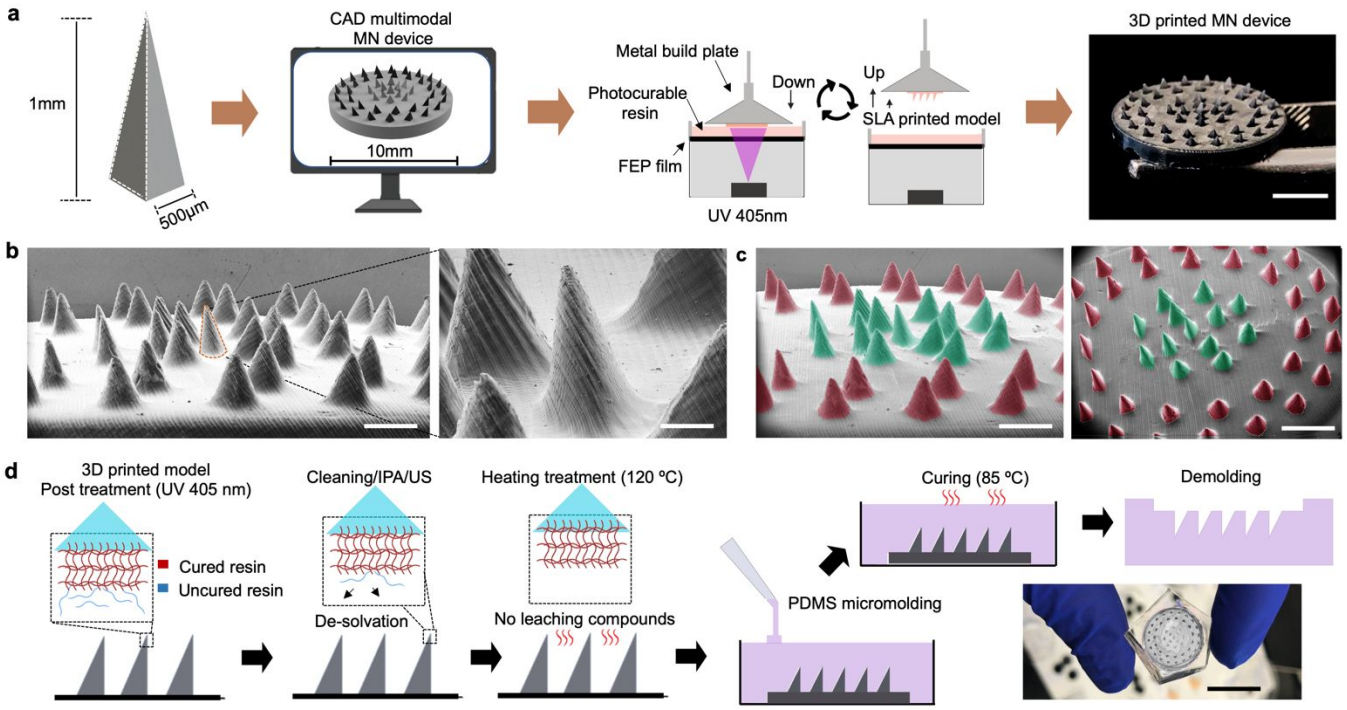

Fig. 2 3D lithographic MN printing. (a) Drafting of the computer aided design (CAD) model of the combinatorial MN patch and lithographic 3D printing process. Digital photograph of 3D-printed MN molds. Scale bar: 2.5 mm. (b) Compositional and morphological analysis of master 3D printed MN molds assessed by SEM. Scale bar, 1mm and 400µm. (c) Colored SEM displaying both distributed compartments within the patch: the fast-acting (green) and sustained release (red) arrays. Scale bars: 1.2 mm and 2 mm, respectively. (d) 3D printed MN array post processing steps: UV treatment, de-solvation and heating, followed by subsequent PDMS micromold fabrication.

An evaluation of different 3D printing parameters to enable controllable dimensions, surface stepping/smoothness and tip sharpness can be found in Table S1 and Table S2 (ESI†). Master MN arrays were subjected to a scanning electron micrograph (SEM) to verify needle quality after each printed

batch; a characteristic SEM of the master combinatorial MN array printed after optimization is shown in Fig. 2b. Additional SEM images of different printing parameters can be found in Fig. S1 and S2 (ESI†). Colored SEM image of the master array clearly depicting the spatially resolved MN compartments is shown in Fig. 2c (fast-acting and sustained MNs in green and red, respectively).

Prior to the fabrication of negative micromolding steps, master MN arrays were subjected to a post processing procedure to remove all leaching compounds inherent from the acrylate resin used in the printing process (Fig. 2d). Leaching compounds demonstrated to inhibit the PDMS curing process, not enabling it to correctly reproduce master mold features, leaving behind not useful silicone molds; molds required to be subjected under UV light (405 nm) and temperature treated for different times (detailed fabrication and parameters in Table S3, ESI†). Following post treatment, silicone negative molds were developed by casting PDMS over post-processed master MN arrays (Fig. 2d).

Tailored fabrication and optimization of dual-stage combinatorial MN patches

We molded combinatorial MNs by casting different materials onto each compartment. Briefly, to prepare fast-acting MNs we proceeded to pack Mg microparticles (30-100μm in diameter) into mold cavities by a drop casting process using a Mg-isopropanol suspension. After the solvent was evaporated, we proceeded to cast an aqueous solution (H_2O, pH 10.5) to solubilize CMC (2, 3 and 4%, w/v) and FITC, enabling a slow evaporation under vacuum during the active compartment fabrication, therefore avoiding Mg particle reactivity (hydrogen bubble generation) throughout the drying process. The cavities designated for sustained release MNs were subsequently filled under vacuum by casting an organic solvent (ethanol/isopropanol, 50:50% v/v) to solubilize Rh6G and Eudragit®L100 (4, 8, 16 and 24%, w/v). After having both MN compartment cavities filled and dried, molds were allocated inside a conventional oven to enhance MN strength. Later, an aqueous and ethanol based polyvinylpyrrolidone (PVP, 10%, w/v) backing solution was applied to the fast-acting and sustained release MN compartments, respectively. The resulting combinatorial MN patch was then transferred to a slightly larger medical adhesive. The patch was custom designed to be small, enabling ease of use, facile transportation and consequently easy storage and handling. Schematics of the steps involved (side and top views) in the fabrication of combinatorial MN patches are illustrated in Fig. 3a (detailed fabrication in ESI†).

Combinatorial MN patches were formulated from different polymer concentrations. Therefore, we decided to examine their dissolution properties by imaging them at different times. Time-frame fluorescence microscopy dissolution images of characteristic fast-acting MN formulations can be found in Fig. 3b. Fast-acting needle dissolution images (30s intervals) with variable concentration (2, 3 and 4% CMC) showed that the polymer matrix is dissolved almost instantly when in contact with the solution (phosphate buffered solution (PBS) pH 7.4). Images clearly show the spontaneous and vigorous H_2 pump activity from the entrapped Mg microparticles as soon as they are exposed to the solution. From this perspective, no significant difference was found within groups examined, as all demonstrated complete MN dissolution within a short period of time displaying rapid particle activation.

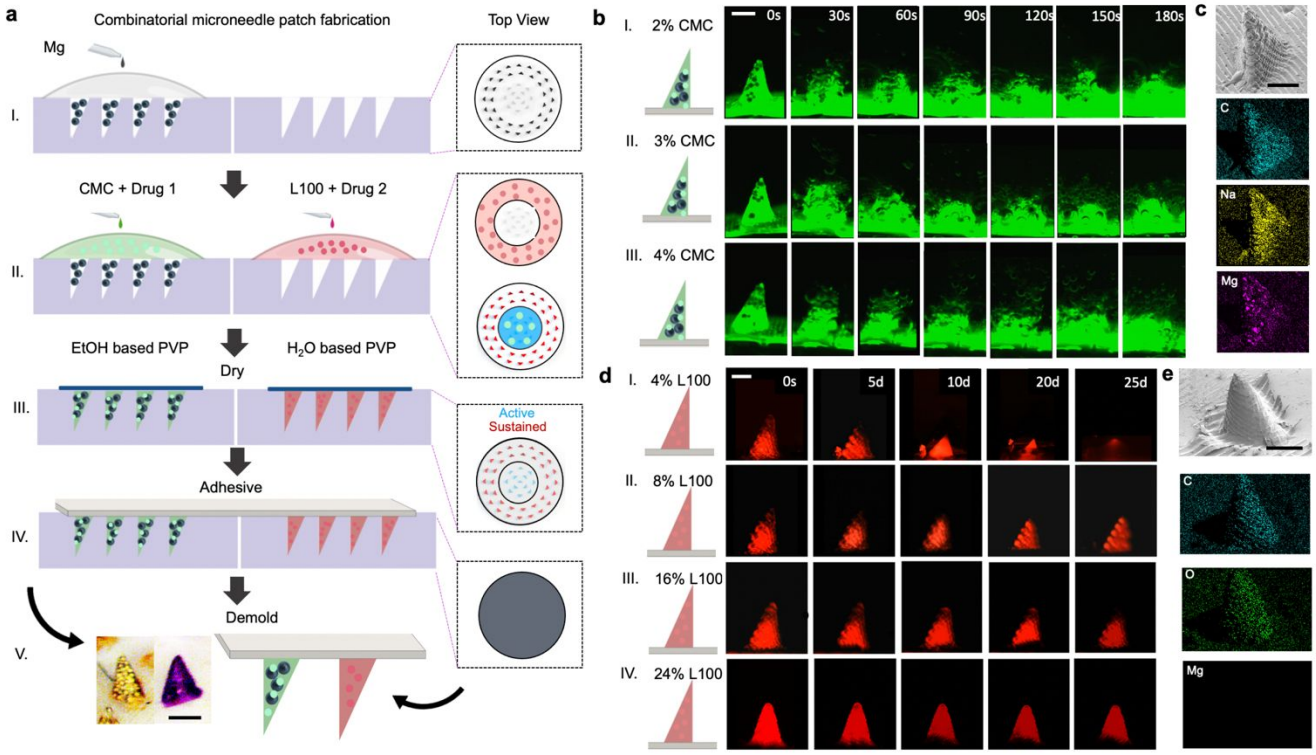

Fig. 3 Dual-stage combinatorial MN patch customization for the simultaneous co-delivery of different drug payloads. (a) Schematics of the steps involved in the fabrication of combinatorial MN patches (side and top view) for the fast-acting and sustained delivery: active particle loading (I), polymer (CMC, Eudragit®L100) and payload inclusion (FITC, Rh6G), respectively (II), polymer base and drying (III), adhesive application (IV) and demolding (V). (b) Fluorescence microscopy time-frame dissolution images of the "fast-acting" MN compartment, displaying a rapid polymer matrix dissolution driven by the reactivity of Mg microparticles (30 s intervals) (I) 2% CMC, (II) 3% CMC, (III) 4% CMC, packed with 1mg of Mg. Scale bar: 400 µm. (c) SEM image of a characteristic fast-acting MN and its corresponding EDX (C,

Na and Mg). Scale bar: 400 µm. (d) Fluorescence microscopy time-frame dissolution images of the "sustained release" MN compartment, displaying slow polymer matrix degradation at day 5, 10, 20 and 25. (I) Eudragit®L100 4%, (II) 8%, (III) 16%, and (IV) 24%. Scale bar: 400 µm. (e) SEM image of a characteristic sustained release MN and its corresponding EDX analysis (C, O and Mg). Scale bar: 400 µm.

A SEM image of a characteristic fast-acting MN is shown in Fig. 3c. Energy Dispersive X-ray (EDX) elemental analysis of the structure displays the MN composition (Fig. 3c); as expected, elemental analysis of Mg show that Mg microparticles remain entrapped within the MN structure. In contrast, sustained release MNs (4, 8, 16 and 24% Eudragit®L100) visually demonstrated to have slow dissolution properties for days while being exposed to circumvent solution around it (Fig. 3d), where the methacrylic acid pH sensitive co-polymer starts to dissolve at pH values above 6.0. Correspondingly, sustained release MNs were characterized by SEM and EDX (Fig. 3e), image shows a smooth MN surface and sharp tip.

MN patch mechanical performance and delivery modulation

To investigate the optimal formulation of the combinatorial MN patch we performed extensive characterization of each compartment. To evaluate whether MNs had sufficient mechanical strength to penetrate the skin, we evaluated the mechanical performance of fast-acting and sustained release MNs under compression (schematic of the experimental setup shown in Fig. 4a). Results demonstrated that the MN strength under compression increased in both fast-acting and sustained release compartments with increasing polymer (CMC/Eudragit®L100) concentration (force displacement curve shown in Fig. 4b and c, respectively), however, no significant difference was found among the three different polymer concentrations used as fast-acting MNs, where 3% CMC was the most optimal formulation, considering polymer solution viscosity and easier fabrication process to fill the silicone negative molds. Moreover, the area under the curve (AUC) of each MN compartment was estimated up to a displacement of 300µm, where the higher the AUC value, the stronger the MN (Fig. 4d). Although combinatorial MN patches with the lowest concentration were weaker, they tolerated compression forces ≥ 0.15 N needle^{-1}, value reported and expected to enable efficient and reliable skin penetration.[54]

To determine until what degree the drug loading capacity and efficiency of the fast-acting MN compartment could be compromised upon different amount of Mg microparticles, we examined 3%

CMC fast-acting MNs loaded with 0, 0.5, 1, 2, and 3mg of Mg microparticles. A UV-vis spectrum of the characteristic model payload (FITC) loaded, and the corresponding calibration curve (inset) is shown in Fig. 4e. Different formulations of fast-acting MNs were fabricated (0, 0.5, 1, 2, and 3 mg of Mg) and subjected to complete dissolution. UV-vis spectrum of the release of these arrays can be found in Fig. 4f and the corresponding number of micrograms loaded in Fig. 4g. As expected, we identified that regardless of the amount of Mg microparticles loaded within the fast-acting MN array, the relative available space to load the drug seems to be compromised and significantly reduced (~47% for 0.5mg of Mg, 49% for 1mg, 64% for 2 mg and 68% for 3mg). However, this experiment set the foundation to precisely tune the amount of drug that needed to be loaded in each patch; by just adjusting the stock payload solution we were able to fix the loading micrograms required per patch for subsequent *in vitro* release kinetics and *ex vivo* penetration studies.

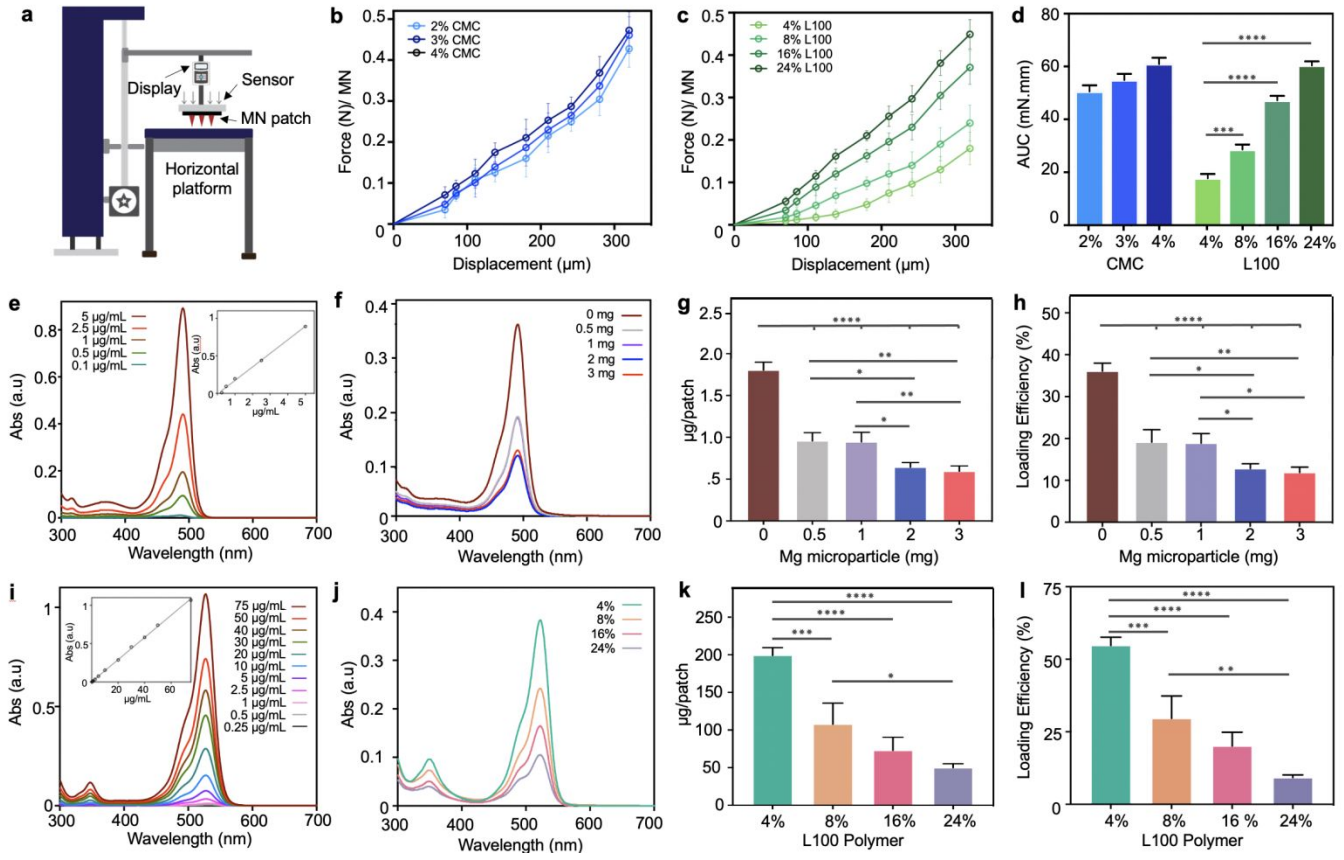

Fig. 4 Mechanical properties, drug loading efficiency and MN compartment optimization. (a) Schematic illustration of the mechanical testing stage employed. (b) Mechanical strength analysis (force displacement curve) of different active MN formulations: 2%, 3% and 4% carboxymethyl cellulose loaded

with 1 mg of Mg microparticles. Points represent means ± s.d (n=5 independent experiments). (c) Mechanical strength analysis (force displacement curve) of diverse sustained release MN formulations: 4%, 8%, 16% and 24% Eudragit®L100. Points represent means ± s.d (n=5 independent experiments). (d) Area under the curve (AUC) up to a displacement of 300 µm. A higher AUC means stronger MN. Data are means ± s.d (n=5). (e) Fast-acting MN patch model payload (FITC) absorbance spectrum calibration curve. (f) Active MN release curves from patches loaded with different amounts of Mg microparticles (0, 0.5, 1, 2 and 3mg). (g) Optimization of the active MN compartment; micrograms of FITC loaded vs Mg microparticle packing. Bars represent means ± s.d (n=5). (h) Active MN compartment loading efficiency vs Mg microparticle packing. Bars represent means ± s.d (n=5). (i) Sustained release compartment MN patch model payload (Rh6G) absorbance spectrum and calibration curve. (j) Sustained release MN release curves from patches fabricated of different MN formulations: 4%, 8%, 16% and 24% Eudragit®L100. (k) Sustained release MN compartment optimization: micrograms of Rh6G loaded vs polymer concentration. Bars represent means ± s.d (n=5). (l) Sustained release MN compartment loading efficiency vs polymer concentration. Bars represent means ± s.d (n=5).Statistical significances were calculated by one-way ANOVA with Tukey's test: **P<0.05, **P<0.01, ***P<0.001, ****P<0.0001.*

Additional graph (Fig. 4h) displays the loading efficiency of each fast-acting patch formulation, where in a very similar manner as they are closely related, the loading efficiency seems to be reduced as the number of milligrams of Mg increase. Likewise, same characterization and optimization experiments were developed to different formulations of sustained release MNs. A UV-vis spectrum of the characteristic model payload (Rh6G) loaded within the sustained compartment, and the corresponding calibration curve (inset) is shown in Fig. 4e. Fabricated MNs (4, 8, 16 and 24% Eudragit®L100) were subjected to complete dissolution. UV-vis spectrum of the release from these arrays is shown in Fig. 4j and the corresponding number of micrograms loaded in Fig. 4k. We identified that the polymer concentration of Eudragit®L100 and the amount of drug that can be loaded in the MN structure are interdependent. As the polymer concentration increases from 4-24%, the number of micrograms loaded per array is significantly reduced (~200µg for 4% L100, ~107µg for 8% L100, ~73µg for 16% L100 and ~50µg for 24% L100). This is expected due to the viscosity increments in the solutions employed (casted within the cavities of the molds) in the fabrication process; where the lower the concentration, the faster the organic solvent vaporization, therefore, higher the loading. Even though the fabrication process of combinatorial MN patches is very well established, the loading will tend to be higher when lower polymer concentrations are employed. Additional loading efficiency graph of sustained release MN compartment (Eudragit®L100) formulations is found in Fig. 4l, clearly displaying the same behavior.

Programmable MN dual-stage active/sustained payload delivery and transdermal penetration

Fluorescence imaging of a characteristic combinatorial MN patch is shown in Fig. 5a. The combinatorial MN patch image is comprised of 3% CMC (1mg/Mg) fast-acting MN and 16% Eudragit®L100 sustained release MN compartments. Fig. 5a(i) shows a combinatorial MN patch before being subjected to dissolution (t=0), clearly displaying both compartments. For convenient visualization, the inner fast-acting needle compartment was loaded with the FITC dye while the outer sustained release needles were loaded with Rh6g. Fig. 5a(ii) displays an image of the same combinatorial MN patch at t=1, where fast-acting MNs are dissolved (t=1) within minutes, leaving behind remaining Mg microparticles in the base of the middle compartment array. Likewise, t=2 (Fig. 5a(iii)) shows the 2nd dissolution stage of the patch, where only the adhesive is left, clearly displaying the complete spatiotemporal dissolution of both compartments.

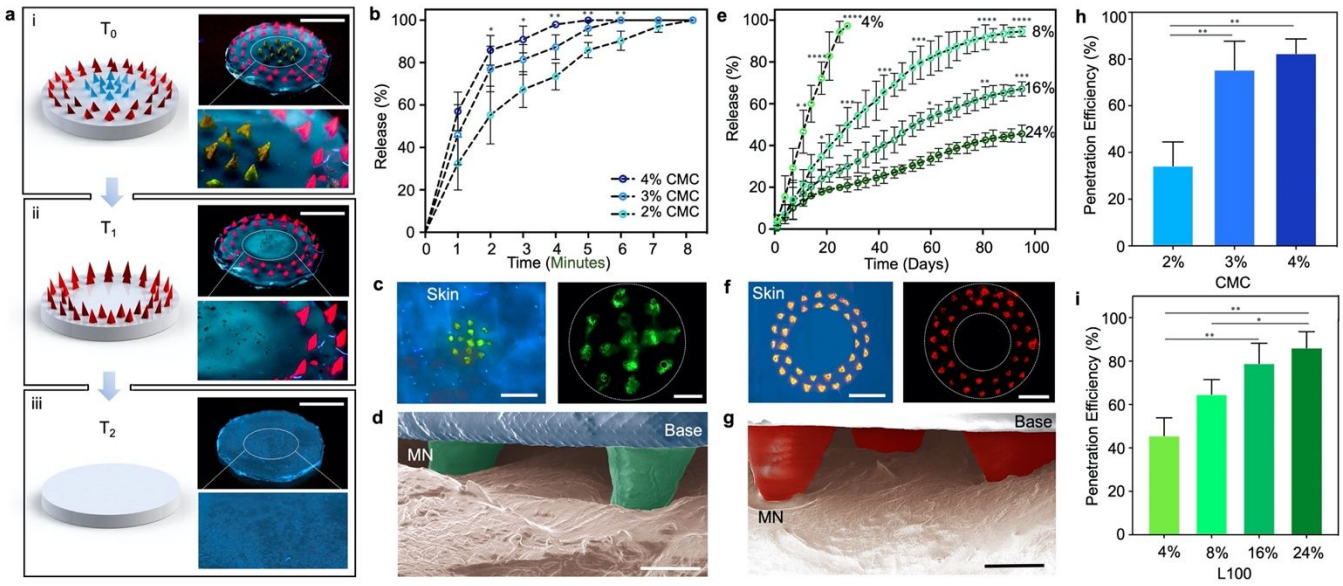

Fig. 5 Dual-stage tunable release kinetics from combinatorial MN patch. (a) Digital fluorescence photographs of the different payload delivery stages at t=0 (Before application), t=1 after active compartment dissolution (burst and fast release of FITC, and t=2 after sustained delivery of Rh6G. Scale bar: 5 mm. (b) Cumulative release kinetic profiles of different formulations of the active MN compartment from the combinatorial MN array, using different CMC loadings (2%, 3% and 4%), showing a fast delivery of FITC over a period of few minutes. Points represent means ± s.d (n=5). (c) Digital photograph of the MN patch onto cadaver porcine skin and subsequent imaging of the skin after application, under UV lamp (left) and fluorescence microscopy imaging under GFP channel (right). Scale bars: 4 and 2 mm, respectively. (d) Colored SEM image depicting an active MN compartment piercing

porcine skin. Scale bar: 500 µm. (e) Tunable cumulative release profile kinetics from the sustained compartment of the combinatorial MN array: the prolonged delivery of Rh6G is achieved from weeks to months (in connection to Eudragit®L100 polymer concentrations of 4%, 8%, 16% and 24%). Points represent means ± s.d (n=5). (f) Digital photograph of sustained release compartment MN after piercing porcine cadaver skin, under UV lamp (left) and fluorescence microscopy imaging under RFP channel (right). Scale bars: 4 and 2.5 mm, respectively. (g) Colored SEM image depicting a sustained MN compartment piercing porcine cadaver skin. Scale bar: 500 µm. (h) Percentage penetration of active MN in porcine skin. Bars represent means ± s.d (n=5). (i) Percentage penetration of sustained release MN in porcine skin. Bars represent means ± s.d (n=5). Statistical significances were calculated by one-way ANOVA with Tukey's test: **P<0.05, **P<0.01, ***P<0.001, ****P<0.0001.*

Dual release kinetics from combinatorial MN patches was performed *in vitro* using release media of saline buffered solution PBS pH 7.4 (chosen to simulate in vivo transdermal pH).[17,57] FITC release from the fast-acting MN compartment (with 2, 3, and 4% CMC) showed a burst release within the first minutes (Fig. 5b). All three patches were fairly consistent over time with no significant difference in release within this short period of time (<8 min). Release percentage of the different patch formulations at 2 min are: 2% CMC (85±7%), 3% CMC (76±10%) and 4% CMC (55±13%) and at 5 min are: 2% CMC (100%), 3% CMC (96±3%) and 4% CMC (85±4%). This data indicates that the fast-acting MN compartment can deliver rapid onset of payloads, achieving the target delivery timeframe in few minutes. The hydrogen generation rate and heat exchange from Mg microparticles strongly depends on the surrounding pH environment (as demonstrated in Fig. S3, ESI†). Such dependence suggests that the heat release from Mg microparticles is small and will not compromise the entrapped payload integrity. The 3% CMC fast-acting MN compartment was manually applied to cadaver porcine skin for a total of 10 min and imaged in Fig. 5c under UV lamp and fluorescence microscopy imaging under green fluorescence protein (GFP) channel. A pseudo-colored SEM image displays the penetration of two fast-acting MNs in green to the skin (Fig. 5d); these images show that MNs penetrated skin efficiently. Furthermore, the release kinetics from the sustained (slow) release MN compartment (4, 8, 16 and 24% Eudragit®L100) showed no initial burst release on day 1 (Fig. 5e), with a constant Rh6G release over time (ranging from ~0.4 to ~3.8% Rh6G release per day, depending on the polymer concentration). By using 4% Eudragit®L100, the payload was released within 28 days, while using higher Eudragit®L100 concentrations resulted in longer time-frame delivery period exceeding 90 days (combinatorial MN release absorbance curves are shown in Fig. S4, supporting information). These release profiles clearly illustrate the ability to tune the sustained release for period ranging from weeks to months through control of the Eudragit®L100 loading. Additional data

on an alternative delivery system by the microencapsulation of Rh6G was developed by synthetizing PLGA microparticles; in contrast to our combinatorial patch, PLGA microparticles deliver full dosages within ~40 days, corresponding data of the release and procedures can be found in Fig. S5 (ESI†). The 16% Eudragit®L100 sustained MN compartment was manually applied to cadaver porcine skin and imaged in Fig. 5f under UV lamp and fluorescence microscopy imaging under RFP channel. Images display that MNs penetrated skin efficiently; additionally, a pseudo-colored SEM image displays the penetration of three fast-acting MNs in red to the skin (Fig. 5g). The combinatorial microneedle composition and design allow the transfer base (PVP) to detach from the needles post application (>10 min) and thus to reduce the risk of infection while increasing patient compliance and leaving behind no sharp waste. (as illustrated in Fig. S6, ESI†). Combinatorial MN patches were applied to porcine skin and the penetration efficiency of both fast-acting and sustained compartments is shown in graph (Fig. 5 h and i, respectively). The 2% CMC/4% L100 composition resulted in penetration efficiency lower than 50% (directly related to the percentage of drug delivered within the skin). Nevertheless, by increasing the polymer concentration, the skin penetration improved, regardless of the polymer used in the fabrication process. The majority of needles were able to breach dermal barriers in an efficient matter, delivering the payload and remained fully embedded under the skin surface. Although our combinatorial MN patches are currently based on manual administration, we plan to develop and use applicators future studies.

Conclusions

We developed a combinatorial MN patch with dual and tunable release kinetics, aimed at providing greater access in delivering wide range of therapeutics with variable target delivery timeframes in a single application. The patch was fabricated to be comprised of two MN compartment zones: a fast-acting and a sustained release compartment. The dual release properties of the patch with different dissolution time frame is attributed to the ability of the patch to load several drugs (even with different solubility and incompatible) within the same array, but spatially resolved, due to the additive manufacturing process employed. MN compartments in such combinatorial array can thus be engineered and tailored to present different release kinetics based on the specific materials and compositions used in fabrication. More encouragingly, we demonstrate that the combinatorial patch can be programmed to deliver drug payloads faster in minutes, greatly enhancing the release when

compared to passive MNs, but additionally, can deliver dosages that last over the course of weeks-to-months, for up to >90 days, with constant release over time. We envision that using different active microengine materials will allow tailoring the burst release profiles of the new ballistic MN. This novel combinatorial MN patch provides flexibility in the loading capacity, as needed to reach clinically relevant doses, and is expected to improve therapeutic efficacy and improve patient compliance towards substantially enhanced pain management. In the absence of effective treatment modalities for neuropathic pain, we envision that the new patch has the potential to improve control of postoperative pain of current therapy platforms, achieving powerful benefits by single patch application, decreasing daily injections, localizing the treatment, thus increasing efficacy. The new concept is expected to benefit a wide range of medical situations, beyond pain management.

Materials and methods

MN CAD/CAM design

Drafting of the computer aided design (CAD) model of the printed part was custom designed in a modeling program (Solidworks version 2019-2020) and ran in an operated Microsoft system-based computer. The microneedle array was designed without considering having PDMS walls between the different MN compartments (microchannels in the master mold), to facilitate the micromolding process of the combinatorial microneedles (easier removal of polymer solution from the base). Models were transferred to a free open-source SLA/DLP/LCD 3D printer software to adjust, prepare and edit the 3D model (Chitubox-Version 1.6.3) prior slicing and printing. Specifically, the developing of supports and lattices for each model with the corresponding dimensions and connections to prevent printing failure. Computer aided manufacturing (CAM) was developed by AnyCubic Photon Slicer Software with the parameters listed in Table 1 and 2.

3D lithographic MN printing

The direct light processing (DLP) fabrication of MNs was developed with the use of an AnyCubic Photon UV LCD 3D Printer. The DLP 3D printer projected a 25W UV light source through a 2K LCD masking photocuring a liquid resin material (black colored AnyCubic acrylate resin). The 3D printed models were mass produced and cured in a layer-by-layer fashion (20-50μm layers). Printed models were removed

from the 115 x 65mm metal build plate and supports trimmed. The MN models were tippled rinsed with 2-propanol (Sigma Aldrich) and further placed within an ultrasonic bath to remove uncured resin material in excess.

MN post processing

Post processing of the printed MN mold was performed by an additional post curing step under a 60W Mercury UV Curing Lamp (Moai Peopoly) for 30 min. Subsequently, MNs in a metal plate (10cm x 10 cm; 2 mm thickness) were heat treated at a fixed temperature (120 ^{o}C) for different times (3-30 min) in a conventional oven. Detailed parameters of post processing are listed in Table S3, supporting information.

PDMS MN micromold fabrication

The polydimethylsiloxane (PDMS) SYLGARD® 184 (Ellsworth Adhesives) micromolding process of 3D printed MNs allowed the fabrication of reusable negative templates for the mass production of combinatorial polymeric MN arrays. The fabrication of silicone MN molds was done by the following procedure: PDMS (12g, 86/14; base/curing agent) solution was casted over a combinatorial MN array attached to a crystal-clear borosilicate petri dish glass. Afterwards, PDMS was degassed in a sealed desiccator connected to a vacuum pump for 15 min at 23 in Hg. PDMS was set to cure (30 min at 85°C) in an oven and further demolded from the master combinatorial MN array, thus obtaining the final combinatorial negative mold. Negative molds were resized with the use of a stainless-steel blade cut and triple cleaned/washed with hand soap; subsequently allocated in an ultrasonic bath, sterilized at 80^{o}C and stored in a sealed container prior use.

PLGA microparticle synthesis

The fabrication method of the Rhodamine 6G (Rh6G, Sigma Aldrich; λex/λem, 526/555 nm)-loaded poly(lactic-co-glycolic acid) (PLGA, MW=50/50, Sigma Aldrich) microparticles was based on an emulsion solvent evaporation technique. Briefly, PLGA (30mg) was dissolved in Ethyl Acetate (1mL, Sigma Aldrich). Subsequently, Rh6G (5mg) was dispersed in the polymer solution, and further poured into a 2% PVA aqueous solution (10mL). Solution was emulsified with the use of a high-speed ultrasonic homogenizer

(Ultrasonics) by three 3s (100W) pulses. The organic phase was allowed to evaporate by continuous mixing (900 rpm) for 18h at ambient temperature. PLGA microparticles were collected by centrifugal force (10,000 rpm) for 7 min and tripled washed with deionized water. Microparticles were suspended in deionized water and then used for MN patch fabrication and particle characterization.

Combinatorial polymeric MN micromolding

The fabrication of the combinatorial (active/sustained) polymeric MN patch was realized by a micromolding approach following the next procedure. The fabrication process of this bi-compartmental specific microneedle array design restricted us in fabricating each polymeric microneedle compartment in a sequential specific form (inner to outer order). Briefly, the compartment designated for the active MNs was primarily loaded and packed with Mg microparticles (0, 0.5, 1, 2, or 3 mg) by employing a 2-propanol Mg microparticle suspension (50 mg mL^{-1}, catalog #FMW40, TangShanWeiHao Magnesium Powder Co., Ltd China), followed by casting a 3% (w/v) sodium carboxymethyl cellulose (CMC, 50 μL, average MW=250K) aqueous polymer solution (pH 10.5 to prevent Mg microparticle reaction and corresponding hydrogen bubbles generation) supplemented with Fluorescein 5(6)-isothiocyanate (FITC, 0.2mg mL^{-1}; λex/λem, 492/518 nm). Molds were allocated under a sealed desiccator connected to a vacuum pump (23 in Hg) for 5 min. Bubbles were removed from the mold and the process was repeated by triplicate. Process was repeated 5 times. Excess of solution was removed from the mold by swiping it with the use of a blade cut and saved for the next repetition. The active compartment was allowed to dry for 15 min between each addition and kept at room temperature for 30 min prior the following compartment fabrication. The procedure of the sustained release compartment fabrication was performed by loading it with a polymeric blend of a 4%, 8%, 16% and 24% (100μL, Ethanol/2-propanol; 50/50% *v/v*) solution of Eudragit®L100 supplemented with Rh6G (0.5mg). Similarly, this allowed us to take advantage of the design and wipe easily the excess of remaining polymer solution from the mold in a circular motion without compromising the previously made compartment and saved for next mold fabrication (process repeated by triplicate). The sustained release compartment was further allowed to dry for 15 min at room temperature. The finished combinatorial MN mold was placed inside a conventional oven for 2h at 70°C. For the cumulative release kinetics experiments a layer of polyvinylpyrrolidone (PVP, MW=360K) was added as a support base on top of the active or sustain

release compartment by casting an ethanol (50 µL, Sigma Aldrich) based or water based (100µL) 10% (w/v) PVP solution respectively and let to dry overnight. Finally, the active/sustained combinatorial MN patch was obtained by a demolding procedure; in brief, after drying, a 1 mm circular adhesive (3M) was adapted to the backing of the MN patches and demolded. The reason behind the PVP layers was to efficiently detach the needles for release measurements and to prove mechanical stability. Prior use, the combinatorial MN patches were stored in a sealed container at room temperature. CMC, PVP, Eudragit®L100 polymer solutions were prepared using a dual asymmetric centrifugal mixer (Flacktek Speedmixer, DAC 150.1 KV-K, FlackTek, SC, U. S. A.), speed of 2500 rpm for 5 min (by triplicate). Combinatorial MN patches loaded with PLGA microparticles were fabricated following the same procedure. Nevertheless, instead of Rhd6G alone, PLGA@Rh6G microparticle suspension (30µL) was infiltrated within the cavities of the silicon molds, and polyvinylpyrrolidone (PVP) was casted on top as the matrix MN material. Even though the polymer matrix is made of a water-soluble material, PLGA@Rh6G microparticles provided sustained release over prolonged periods of time.

MN patch imaging characterization

Fluorescent microscopy images of the combinatorial MN patches were developed with the use of a fluorescent microscope (EVOS FL coupled with 2x and 4x objectives and GFP and RFP filters) for the imaging of Rh6G and FITC. SEM images were performed by a FEI Quanta 250 ESEM instrument (Hillsboro, Oregon, USA). Prior imaging, the 3D printed, and polymeric combinatorial MN patches were sputtered with Iridium in an Emitech K575X Sputter Coater, providing a fine grain metal deposition; samples were imaged at acceleration voltages between 3-5 keV. Bright field and colored images were obtained by a 3.5X-180X Simul-Focal Stereo Zoom Microscope coupled with an 18MP digital camera. Digital fluorescent images of the combinatorial MN patch before and after dissolution were carried out with a digital camera Nikon D7000 coupled with a 40mm 2.8G macro lens; MN patches were placed under a portable UV lamp projecting a 365nm wavelength light.

MN patch dissolution experiments

To image the dissolution in solution of our combinatorial MN, 3 continuous MN (active or sustained, loaded with FITC or Rh6G, respectively) were attached horizontally to a clear glass slide with 4 acrylate walls to contain solution. To capture the dissolution in real time, Phosphate buffered solution (pH 7.4)

was administrated to the MN setup, followed by time-set point frame images with use of a fluorescent microscope (EVOS FL coupled with a 4x objective and GFP-RFP filters).

MN patch mechanical strength study

Fast-acting and sustained release MN arrays from the patch were set under a mechanical compression test. The set up used was comprised of a Force Gauge Model M4-20 system Mark0-10 Series 4, a metal plate and a stepping-motor controlled biaxial stage. In brief, each MN array was set under a constant load, and the displacement of the base plate in reference to each needle height was monitored and plotted. The fracture (failure) force was determined by a notorious drop in force.

Release Kinetics Experiments

Fast-acting and sustained release MN patches were subjected to a release kinetics study. MN patches were dissolved in 1000 µL of PBS pH 7.4 at 37.5 °C for different set-time points: the fast-acting MN (from 1-10 min) and sustained release compartment (from 1-90 days). Prior each measurement samples were centrifuged at 4000 rpm for 5 min, and the solution release amount was measured by UV-vis spectrophotometry (UV-2450 Shimadzu spectrophotometer) in an average of 3-4 days. After each measurement, 1mL of PBS pH 7.4 solution was replaced within the sealed container. Each measurement was conducted within a 400-700 nm spectrum window. The patches release was plotted vs time. Data was analyzed and charts were generated using Prism 7 (GraphPad software).

PLGA-Rh6G microparticle release study

PLGA@Rh6G microparticles were dissolved in 1000 µL of PBS pH 7.4 at 37.5 °C for different set-time points: (from 1-45 days). Prior to each measurement, samples were centrifuged at 4000 rpm for 5 min and the release amount was measured by UV-vis spectrophotometry (UV-2450 Shimadzu spectrophotometer). Each measurement was conducted within a 400-700 nm spectrum window. Particle release was plotted vs time. Data was analyzed and charts were generated using Prism 7 (GraphPad software).

Skin Penetration Studies

Both fast-acting and sustained release MN patches were set to pierce porcine cadaver skin. The skin thickness was sliced to be ~3.0mm in thickness and was stored in a sealed container with PBS (pH 7.4) at room temperature prior use. The combinatorial MN patches were applied to the skin manually.

Conflicts of interest

The authors declare no conflict of interest

Acknowledgements

This work was supported by the NSF grant 1937653 to J.W. and by the UCSD Center of Wearable Sensors. M.A.-L.R., F.S. and M.R acknowledge the UC MEXUS-CONACYT Doctoral Fellowships. L. M acknowledges FAPESP fellowship 2019/16608-4TOC. Some schematics were created with biorender.com.

References

1 E. Larrañeta, M.-T. McCrudden, A.-J. Courtenay and R.-F. Donnelly, *Pharm. Res.,* 2016, **33**, 1055–1073.

2 D.-D. Zhu, X.-P. Zhang, B.-L. Zhang, Y.-Y. Hao and X.-D. Guo, *Adv. Ther.,* 2020, **3**, 2000033.

3 H. Lee, T.-K. Choi, Y.-B. Lee, H.-R. Cho, R. Ghaffari, L. Wang, H.-J. Choi, T.-D. Chung, N. Lu, T. Hyeon and S.-H. Choi, *Nat. Nanotechnol*., 2016, **11**, 566–572.

4 W. Chen, R. Tian, C. Xu, B.-C. Yung, G. Wang, Y. Liu, Q. Ni, F. Zhang, Z. Zhou, J. Wang and G. Niu, Nat. Commun., 2017, **8**, 1777.

5 R. Jamaledin, C.-K. Yiu, E.-N. Zare, L.-N. Niu, R. Vecchione, G. Chen, Z. Gu, F.-R. Tay and P. Makvandi, *Adv. Mater*., 2020. **32**, 2002129.

6 M. Yin, L. Xiao, Q. Liu, S.-Y. Kwon, Y. Zhang, P.-R. Sharma, L. Jin, X. Li and B. Xu, *Adv. Healthc. Mater*., 2019, **8**, 1901170.

7 X. Xie, C. Pascual, C. Lieu, S. Oh, J. Wang, B. Zou, J. Xie, Z. Li, J. Xie, D.-C. Yeomans and M.-X. Wu, *ACS nano,* 2017, **11**, 395–406

8 J. Arya and M.-R. Prausnitz, *J. Control. Release,* 2016, **240**, 135–141.

9 H. Lee, C. Song, S. Baik, D. Kim, T. Hyeon and D.-H. Kim, *Adv. Drug Deliv. Rev.,* 2018, **127**, 35–45.

10 K. Van der Maaden, W. Jiskoot and J. Bouwstra, *J. Control. Release,* 2012, **161**, 645–655.

11 S. Marshall, L. J. Sahm and A. C. Moore, *Hum. Vaccin. Immunother*., 2016, **12**, 2975–2983.

12 J.-J. Norman, J.-M. Arya, M.-A. McClain, P.-M. Frew, M.-I. Meltzer and M.-R. Prausnitz, *Vaccine*, 2014, **32**, 1856–1862.

13 N.-G. Rouphael, M. Paine, R. Mosley, S. Henry, D.-V. McAllister, H. Kalluri, W. Pewin, P.-M. Frew, T. Yu, N.-J. Thornburg, S. Kabbani, L. Lai, E.-V. Vassilieva, I. Skountzou, R.-W. Compans, M.-J. Mulligan and M.-R. Prausnitz, *Lancet,* 2017, **390**, 649–658.

14 S. Bhatnagar, K. Dave and V.-V.-K. Venuganti, *J. Control. Release,* 2017, **260**, 164–182.

15 T.-A. Petukhova, L.-A. Hassoun, N. Foolad, M. Barath and R.-K. Sivamani, *JAMA Dermatol*., 2017, **153**, 637–643.

16 R.-F. Donnelly, D.-I. Morrow, M.-T. McCrudden, A.-Z. Alkilani, E.-M. Vicente-Pérez, C. O'Mahony, P. González-Vázquez, P.-A. McCarron and A.-D. Woolfson, *Photochem. Photobiol.,* 2014, **90**, 641–647.

17 R.-F. Donnelly, T.-R.-R. Singh, M.-J. Garland, K. Migalska, R. Majithiya, C.-M. McCrudden, P.-L. Kole, T.-M.-T. Mahmood, H.-O. McCarthy and A.-D. Woolfson, *Adv. Funct. Mater.,* 2012, **22**, 4879–4890.

18 Y.-C. Ryu, D.-I. Kim, S.-H. Kim, H.-M.-D. Wang and B.-H. Hwang, *Biotechnol. Bioprocess Eng*., 2018, **23**, 286–292.

19 M.-T. McCrudden, A.-Z. Alkilani, A.-J. Courtenay, C.-M. McCrudden, B. McCloskey, C. Walker, N. Alshraiedeh, R.-E. Lutton, B.-F. Gilmore, A.-D. Woolfson and R.-F. Donnelly, *Drug Deliv. Transl. Res*., 2015, **5**, 3–14.

20 C. Wang, Y. Ye, G.-M. Hochu, H. Sadeghifar and Z. Gu. *Nano Lett.,* 2016, **16**, 2334–2340.

21 P.-C. DeMuth, X. Su, R.-E. Samuel, P.-T. Hammond and D.-J. Irvine, *Adv. Mater*., 2010, **22**, 4851–4856.

22 U. Angkawinitwong, A.-J. Courtenay, A.-M. Rodgers, E. Larrañeta, H.-O. McCarthy, S. Brocchini, R.-F. Donnelly and G.-R. Williams, *ACS Appl. Mater. Interfaces,* 2020, **12**, 12478–12488.

23 X. Lan, J. She, D.-A. Lin, Y. Xu, X. Li, W.-F. Yang, V.-W.-Y. Lui, L. Jin, X. Xie, Y.-X. Su, *ACS Appl. Mater. Interfaces,* 2018, **10**, 33060–33069.

24 J.-H. Park, M.-G. Allen and M.-R. Prausnitz, *Pharmaceutical research*, 2006, **23**, 1008–1019.

25 Y. Zhang, Q. Liu, J. Yu, S. Yu, J. Wang, L. Qiang and Z. Gu, *ACS nano*, 2017, **11**, 9223–92030.

26 W. Li, R.-N. Terry, J. Tang, M.-R. Feng, S.-P. Schwendeman and M.-R. Prausnitz, *Nat. Biomed. Eng.,* 2019, **3**, 220–229.

27 W. Li, J. Tang, R.-N. Terry, S. Li, A. Brunie, R.-L. Callahan, R.-K. Noel, C.-A. Rodríguez, S.-P. Schwendeman and M.-R. Prausnitz, *Sci. Adv.,* 2019, **5**, eaaw8145.

28 A.-V. Boopathy, A. Mandal, D.-W. Kulp, S. Menis, N.-R. Bennett, H.-C. Watkins, W. Wang, J.-T. Martin, N.-T. Thai, Y. He, W.-R. Schief, P.-T. Hammond and D.-J. Irvine, *PNAS*, 2019, **116**, 16473–16478.

29 S. Wang, M. Zhu, L. Zhao, D. Kuang, S.-C. Kundu and S. Lu, *ACS Biomater. Sci. Eng*., 2019, **5**, 1887–1894.

30 H. Kathuria, D. Lim, J. Cai, B.-G. Chung and L. Kang, *ACS Biomater. Sci. Eng.*, 2020, **6**, 5061–5068.

31 K.-T.-M. Tran, T.-D. Gavitt, N.-J. Farrell, E.-J. Curry, A.-B. Mara, A. Patel, L. Brown, S. Kilpatrick, R. Piotrowska, N. Mishra, S.-M. Szczepanek and T.-D. Nguyen, *Nat. Biomed. Eng*., 2020, DOI 10.1038/s41551-020-00650-4

32 Z. Wang, J. Wang, H. Li, J. Yu, G. Chen, A.-R. Kahkoska, V. Wu, Y. Zeng, D. Wen, J.-R. Miedema, J.-B. Buse and Z. Gu, *PNAS,* 2020, **117**, 29512–29517.

33 M. C. Chen, S. F. Huang, K. Y. Lai, and M. H. Ling, *Biomaterials*, 2013, **34**, 3077–3086.

34 P. C. DeMuth, Y. Min, D. J. Irvine, and P. T. Hammond, *Adv. Healthc. Mater*., 2014, **3**, pp.47–58.

35 Y. Gao, M. Hou, R. Yang, L. Zhang, Z. Xu, Y. Kang and P. Xue, *Macromol. Mater. Eng.*, 2018, **303**, 1800233.

36 E. Drucker, P.-G. Alcabes and P.-A. Marx, *Lancet,* 2000, **358**, 1989–1992.

37 D. Ding, J. Pan, S. H. Lim, S. Amini, L. Kang, and A. Miserez, *J. Mater. Chem. B*, 2017, **5**, 8467–8478.

38 C. Di Natale, D. De Rosa, M. Profeta, R. Jamaledin, A. Attanasio, E. Lagreca, P. L. Scognamiglio, P. A. Netti and R. Vecchione, *J. Mater. Chem. B*, 2021, **9**, 392–403.

39 M.-A. Lopez-Ramirez, F. Soto, C. Wang, R. Rueda, S. Shukla, C. Silva-Lopez, D. Kupor, D.-A. McBride, J.-K. Pokorski, A. Nourhani, N.-F. Steinmetz, N.-J. Shah and J. Wang, *Adv. Mater.,* 2020*,* **32***,* 1905740.

40 C.-E. Boone, C. Wang, M.-A. Lopez-Ramirez, V. Beiss, S. Shukla, P.-L. Chariou, D. Kupor, R. Rueda, J. Wang and N.-F. Steinmetz, *ACS Appl. Nano Mater*., 2020, **3**, 8037–8051.

41 B. Esteban-Fernández de Ávila, P. Angsantikul, J. Li, M. A. Lopez-Ramirez, D. E. Ramírez-Herrera, S. Thamphiwatana, C. Chen, J. Delezuk, R. Samakapiruk, V. Ramez, M. Obonyo, Z. Liangfang and J. Wang, *Nat. Comm*. 2017, **8**, 1–9.

42 A. Nourhani, E. Karshalev, F. Soto, and J. Wang, *Research*. *2020,* **2020**,1–9.

43 A. Devers and B.-S. Galer, *Clin. J. Pain*, 2000, **16**, 205–208.

44 J. Kennedy, J.-M. Roll, T. Schraudner, S. Murphy and S. McPherson, *J. Pain*, 2014, **15**, 979–984.

45 B. Mandal, D. Das, A.-P. Rameshbabu, S. Dhara and S. Pal, *RSC Adv.,* 2016, **6**, 19605–19611.

46 K. Bekkour, D.-S. Waterhouse and S.-S. Wadhwa, *Food Res. Int.,* 2014, **66**, 247–256.

47 R. Biswal and R.-P. Singh, *Carbohydr. Polym.,* 2004, **57**, 379–387.

48 Y. Chenga, B. Fengb, X. Yanga, P. Yanga, Y. Dinga and Y. Chena, *Sens. Actuators, B.*, 2013, **182**, 288–293.

49 B. Mukherjee, S. Mahapatra, R. Gupta, B. Patra, A. Tiwari and P. Arora, *Eur. J. Pharm*., 2005, **59**, 475–483.

50 P. Minghetti, A. Casiraghi, F. Cilurzo and L. Montanari, *Eur. J. Pharm.*, 2000, **10**, 111–117.

51 S. Tokunaga, K. Ono, S. Ito, T. Sharmin, T. Kato, K. Irie, K. Mishima, T. Satho, T. Harada, T.-M. Aida and K. Mishima, *J. Supercrit. Fluids*, 2021, **167**, 105044.

52 M. Cetin, A. Atila and Y. Kadioglu, *AAPS PharmSciTech.,* 2010, **11**, 1250–1256.

53 B. Esteban-Fernández de Ávila, M.-A. Lopez-Ramirez, R. Mundaca-Uribe, X. Wei, D.-E. Ramírez-Herrera, E. Karshalev, B. Nguyen, R.-H. Fang, L. Zhang and J. Wang, *Adv. Mater*., 2020, **32**, 2000091.

54 X. Lan, W. Zhu, X. Huang, Y. Yu, H. Xiao, L. Jin, J.-J. Pu, X. Xie, J. She, V.-W.-Y. Lui and H.-J. Chen, Nanoscale, 2020, **12**, 18885–18898.

55 M. Wang, Y. Han, X. Yu, L. Liang, H. Chang, D.-C. Yeo, C. Wiraja, M.-L. Wee, L. Liu, X. Liu and C. Xu, *Adv. Healthc. Mater*., 2020, **9**, 1900635.

56 M.-R. Prausnitz, *Adv. Drug Deliv. Rev.,* 2004, **56**, 581–587.

57 L. Wang, Z. Fan, J. Zhang, Y. Changyi, C. Huang, Y. Gu, Z. Xu, Z. Tang, W. Lu, X. Wei and C. Li, *Int. J. Cancer,* 2015, **136**, E107